Bioinspired 3D-Printed Auxetic Structures with Enhanced Fatigue Behavior

Masoud Shirzad [a], Juhyun Kang [b], Garin Kim [a], Mahdi Bodaghi [c], Seung Yun Nam [a,d,]*

[a] *Industry 4.0 Convergence Bionics Engineering, Pukyong National University, Busan 48513, Korea*

[b] *Department of Biomedical Engineering, Pukyong National University, Busan 48513, Korea*

[c] *Department of Engineering, School of Science and Technology, Nottingham Trent University, Nottingham, NG11 8NS, UK*

[d] *Major of Biomedical Engineering, Division of Smart Healthcare, Pukyong National University, Busan 48513, Korea*

E-mail: synam@pknu.ac.kr

Keywords: bioinspired auxetics, fatigues, finite element method, metamaterials, tissue scaffolds

Recently, auxetic metastructures have gained considerable attention in various fields of study due to their unique characteristics. This study aims to design and fabricate bioinspired auxetic structures and comprehensively investigate the static and dynamic mechanical properties of those architectures under tensile and compressive loads. A comparative analysis is carried out with a conventional structure, considering static tensile and compressive tests, as well as dynamic tension–tension and compression–compression assessments. Experimental measurements and finite-element analysis are utilized to evaluate various parameters of the scaffolds, such as Young's modulus, yield strength, energy absorption, stress distribution, Poisson's ratio, and fatigue properties. The findings reveal that bioinspired auxetic structures can appropriately mimic the physical attributes and stress–strain characteristics of human tissue, such as the Achilles tendon. Furthermore, these bioinspired auxetic structures significantly enhance the cycles to failure compared to conventional structures, accompanied by notable improvements in energy absorption. Among the auxetic structures, the star configuration exhibits remarkable tolerance to tensile

fatigue loads, while the sharp sinus structure demonstrates the highest tolerance to cycles to failure under compression–compression loads. The static and fatigue properties of bioinspired auxetic structures indicate their potential for biomedical applications.

1. Introduction

In recent years, the scientific community has been actively engaged in the design of structures with unique properties. One intriguing class of structures is auxetic structures, characterized by possessing a negative Poisson's ratio (NPR). These structures exhibit lateral expansion under tension and densification under opposing loads [1]. One of their most important features is high anisotropy, which can enhance energy absorption capabilities [2]. Additionally, auxetic structures exhibit high permeability and fracture toughness, further contributing to their unique properties [3]. Consequently, these distinctive merits of auxetic structures have found various applications in diverse fields, such as aerospace engineering, running shoes, and biomedical implants [4].

In the realm of biomedical implants, auxetic structures have garnered significant appeal and widespread use due to their ability to improve important features such as longevity and elastic modulus. Certain organs in the human body display a high level of auxeticity and anisotropy, necessitating the implementation of auxetic structures to accurately mimic their physical behavior [5]. For instance, the Achilles tendon exhibits an exceptionally low NPR value of -1.44, rendering conventional scaffolds with a normal positive Poisson's ratio inadequate for replicating the auxetic behavior of this particular tissue [6]. Hence, conventional designs employing irregular pore architectures fall short of guaranteeing the NPR characteristics in scaffolds [7]. Moreover, organs exhibit varying degrees of auxeticity, spanning a range of NPR values from -0.1 to -3. Therefore, it is essential to develop diverse auxetic architectures to suitably match NPR structures to specific organs or tissues [6a].

Previous studies have attempted to mimic natural tendons by incorporating crimped, re-entrant, and random structures but have neglected to design tissue-specific structures achieving high negative Poisson's ratio values [8]. Moreover, in biomedical implants, including bone and tendon substitutes, failure is not primarily caused by static constant loads but is often triggered by cyclic loading, leading to the formation of fatigue cracks within their structures [9]. While the mechanical properties of materials are critical in understanding the fatigue failure of 3D structures, the porous architecture also plays a significant role in controlling fatigue within porous media [10].

Nonetheless, the process of fatigue testing proves to be time-consuming and costly. In response, the finite element method (FEM) offers a numerical approach to predict the mechanical properties of porous structures, reducing the need for extensive experimental investigation. Furthermore, FEM can provide valuable insights by visualizing the stress distribution and deformation, facilitating a comprehensive analysis of the specific structure suitable for biomedical applications. It also elucidates reasons why certain 3D structures may experience failure compared to others, offering a deeper understanding of the underlying mechanics [11]. Therefore, both the static and dynamic mechanical properties of scaffolds can be predicted using the FEM to visualize the stress distribution in the scaffolds [6b, 12].

In addition to the auxetic structure design and simulation techniques, a high level of fabrication of intricate architecture is crucial to developing substitutes with NPR characteristics. However, conventional fabrication techniques, such as injection molding and subtractive manufacturing, are limited in their ability to precisely mimic such complex architectures required to implement NPR. Additive manufacturing offers a viable solution for fabricating complicated 3D microenvironments using a layer-by-layer deposition of materials based on a pre-designed path [12b, 13]. Among various additive manufacturing techniques, fused deposition modeling (FDM) stands out as the most extensively employed method for fabricating tissue-mimicked scaffolds due to its cost-effectiveness and precise control of internal architectures [14].

Combining 3D printing with dynamic load assessment offers a promising approach to bridge the gap in biomimicry and provide a comprehensive evaluation of tissue-specific architectures possessing applicable mechanical and physical properties for organs exhibiting auxetic behavior. Hence, the present study aims to design, fabricate, and evaluate bioinspired auxetic structures to enhance fatigue behaviors in the tissue substitutes, following the procedural framework outlined in Figure 1. In this regard, three bioinspired auxetic architectures, in addition to a conventional structure, were designed, fabricated through 3D printing techniques, simulated using FEM, and mechanically assessed under both static and dynamic loading conditions.

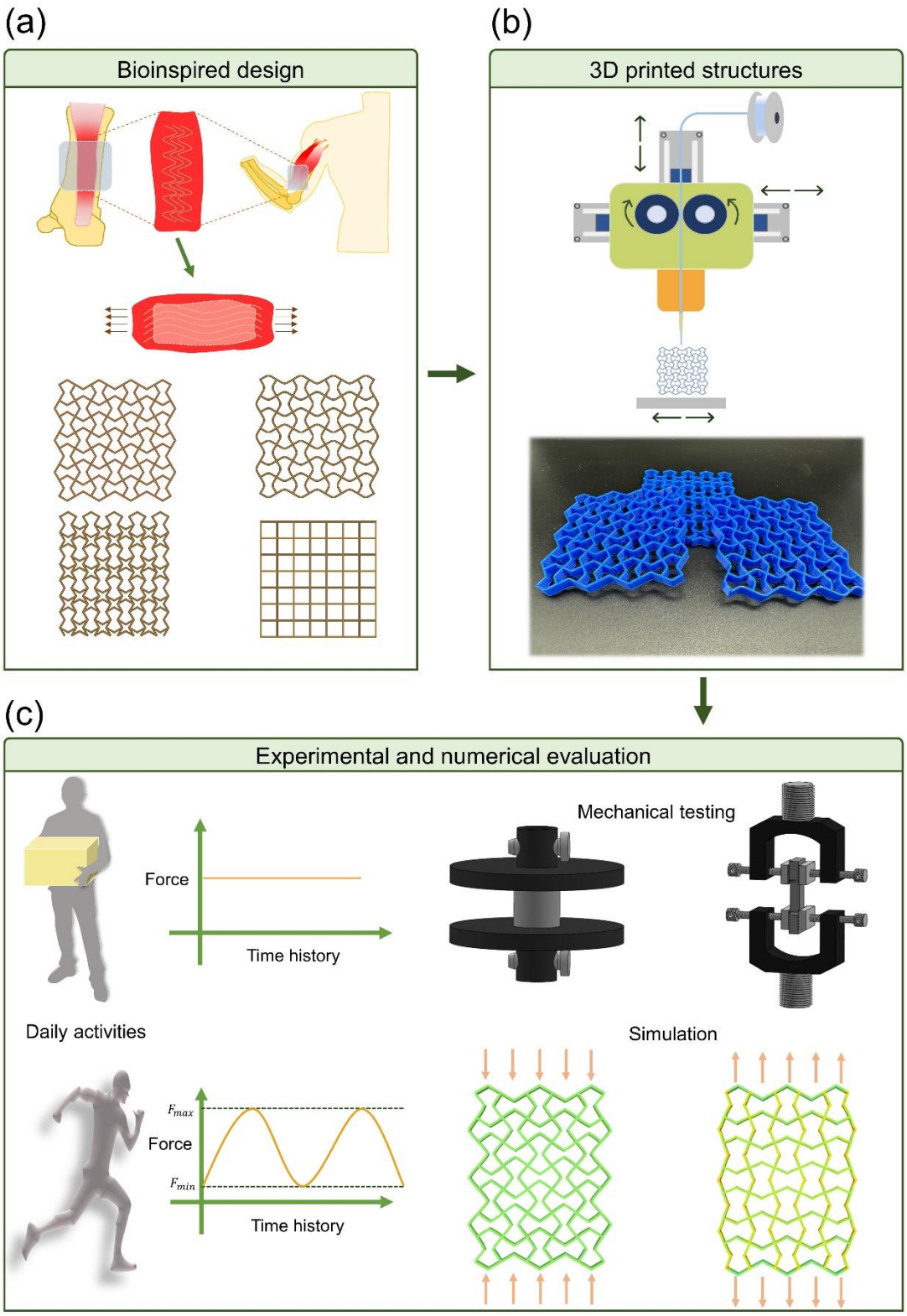

Figure 1. Design, fabrication and evaluation of scaffolds with conventional and auxetic structures: (a) bioinspired design, (b) 3D printed structures, and (c) experimental and numerical evaluation.

Specifically, the loading conditions were categorized into four major groups. Initially, the 3D printed structures were evaluated under static tensile and compressive loads, and the experimental tests served to validate FEM results and determine the stress distribution within various designs. Additionally, the study aimed to bridge the gap by investigating the fatigue behavior of auxetic and conventional structures, comparing their dynamic responses under tension-tension and compression-compression tests.

Based on the NPR properties of the human tendon, it is anticipated that auxetic structures can more accurately mimic the tensile behavior in tendons, which can lead to superior energy absorption and a higher number of cycles to failure compared to the conventional architecture. Hence, both the static and dynamic tests were simulated using FEM, facilitating a comprehensive investigation into the impact of the external loads on the conventional and auxetic scaffolds. Through the integrated approach, combining 3D printing, FEM simulations, and mechanical assessments under diverse loading conditions, the study aims to significantly advance our understanding of bioinspired auxetic structures and their potential applications as tissue substitutes.

2. Results and Discussion

In this study, three types of auxetic structures (SS (sharp sinus), CS (curved sinus), and ST (star)) and one conventional design (CR (conventional rectangular)) were fabricated using 3D printing and evaluated along with experimental and numerical methods. The porosity of the scaffolds was carefully controlled between 70% and 85% to minimize the impact of porosity on their mechanical properties and ensure their suitability for tissue engineering applications. The primary objective was to comprehensively investigate the mechanical characteristics of both auxetic and conventional structures when subjected to static and dynamic loading conditions. Of significant novelty was the exploration of the fatigue performance of polymeric scaffolds for biomedical applications, underscored by a comparative analysis with conventional architecture where tensile and compression loads prevail.

2.1. Static Tensile and Compressive Properties of Scaffolds

The 3D printing method and PLA material were employed to fabricate various auxetic and conventional structures, and their static mechanical properties were evaluated under tension and compression. The stress-strain curves and detailed tensile and compression properties are presented in Figure 2 and Table 1, respectively. Notably, the conventional rectangular scaffold

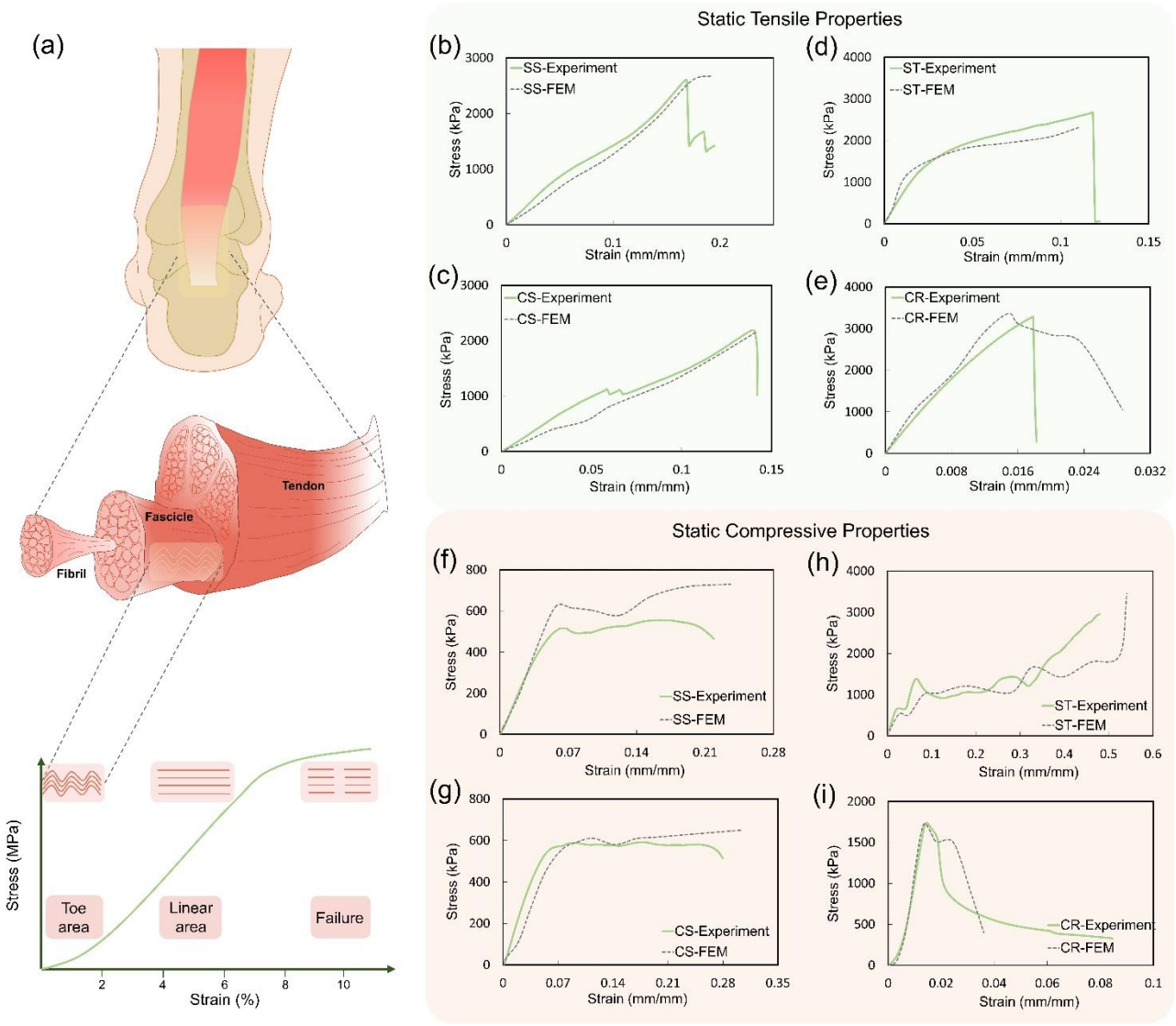

Figure 2. (a) Anatomic illustration and mechanical properties of natural tendon [15]. Static tensile properties and FEM verification of (b) SS, (c) CS, (d) ST, and (e) CR structures. Static compressive properties and FEM verification of (f) SS, (g) CS, (h) ST, and (i) CR structures. Abbreviations: SS, sharp sinus; CS, curved sinus; ST, star; CR, conventional rectangular.

Table1. Static mechanical and physical properties of SS, CS, ST, and CR scaffolds under tensile and compressive loading.

Structure	SS	CS	ST	CR
T- Young's modulus (MPa)	17.23	19.06	66.12	245.55
C- Young's modulus (MPa)	10.54	12.74	35.41	98.51
T-maximum stress (MPa)	2.63	2.18	2.67	3.26
C-yield strength (MPa)	0.51	0.53	0.65	1.67
Porosity (%)	81.3	80.8	70.5	82.3
Poisson's ratio	-1.11	-1.05	-0.45	0.013
T-energy absorption (J/g)	69.49	46.81	47.75	25.37
C-energy absorption (J/g)	24.12	29.93	64.86	14.5

Abbreviations: SS, sharp sinus; CS, curved sinus; ST, star; CR, conventional rectangular; T-Young's modulus, tensile Young's modulus; C- Young's modulus: compression Young's modulus; T-yield strength, tensile yield strength; C-yield strength, compression yield strength.

Table 2. Experimental Poisson's ratio of the tendon in the plane parallel to the surface of the bone [6a].

Tendon	Sample number	Poisson's ratio
Achilles	1	-1.44

	2	-0.39
Peroneus brevis	1	-3.81
	2	-0.166
Deep flexor (ovine)	1	-2.23
	2	-1.14
	3	-0.37
	4	-3.56
	5	-9.86
Deep flexor (porcine)	1	-0.56
	2	-0.34
	3	-3.11
	4	-1.32
	5	-1.32

exhibited the highest Young's modulus and yield strength in both tensile and compression assessments but displayed the lowest energy absorption, low strain capacity, and constrained expansion potential. The maximum strain values in the tensile test were not extensively different in all four samples. However, the auxetic structures, particularly SS and CS designs, demonstrated remarkable strain tolerance and significantly higher energy absorption, up to 2.7 times more than the conventional structure, as shown in Table 1. The SS structure, in particular, exhibited an energy absorption of 59.49 J/g with 81.3% porosity. Interestingly, the tensile pattern of the SS structure closely followed the stress-strain pattern of natural tendons under tensile load (Figure 2a and b). Furthermore, the tendon naturally exhibits auxeticity (negative Poisson's ratio) when stretched up to 2% along its length. The measured Poisson's ratios of the SS, CS, and ST structures, as presented in Table 1, closely align with those observed in human tendons, indicating that these fabricated scaffolds can effectively mimic the deformation patterns of native tissues with auxetic structures, as further supported by the data in Table 2 [6a]. Notably, the obtained Poisson's ratios of the

fabricated scaffolds fall within the range exhibited by various tendons, including the Achilles tendon, which is known to have NPR values between -0.39 and -1.44.

In the compression tests, similar to the tensile experiments, the CR scaffold showed the highest compressive mechanical properties, yet it displayed limited tolerance to high strain, deforming with small changes in dimension, as depicted in Figure 2e and i. In contrast, the auxetic structures exhibited high energy absorption and remarkable tolerance to high strain. Their negative Poisson's ratio allowed them to contract in the transverse direction, leading to enhanced energy absorption (Figure 2f, g, and h). Comparing the three auxetic structures of SS, CS, and ST, the ST structure displayed the highest energy absorption, making it a promising candidate for cancellous bone scaffolds. Notably, the hierarchical architecture of the ST structure closely mimicked natural bone tissue. In the initial stage of the stress-strain curve presented in Figure 2h, the sinusoidal architecture of the ST structure mainly withstood compressive loads. As compressive loads increased, the star unit cells decreased the porosity, subsequently increasing the mechanical properties of the scaffold. It is known that cancellous bone exhibits a low level of auxeticity, with normal mechanical properties ranging from 10 MPa to 2 GPa for Young's modulus and 0.2 MPa to 80 MPa for yield strength [16], aligning with the findings of this study. Additionally, the porosity of cancellous bone scaffolds typically falls between 70% and 90% [17], consistent with the parameters in the present study. Moreover, the strain hardening phenomenon was observed in auxetic structures (Figure 2f, g, and h). As compressive loads increased in auxetic structures, their struts moved inward, creating high-density areas. This adaptation supported the high level of compressive loads, which plays an important role in the load-bearing behavior of bone scaffolds, as shown in Figure 3. However, the CR structure displayed a strain-softening behavior under compressive loads and deformed under low strain values. Among auxetic structures, the ST architecture demonstrated the highest strain hardening due to the compactness of its struts. The fabricated auxetic structures in this study met the requirements for bone tissue engineering applications with suitable porosity, Young's modulus, and yield strength. Also, they showed strain hardening under compressive loads, making them potentially suitable for bone scaffolds.

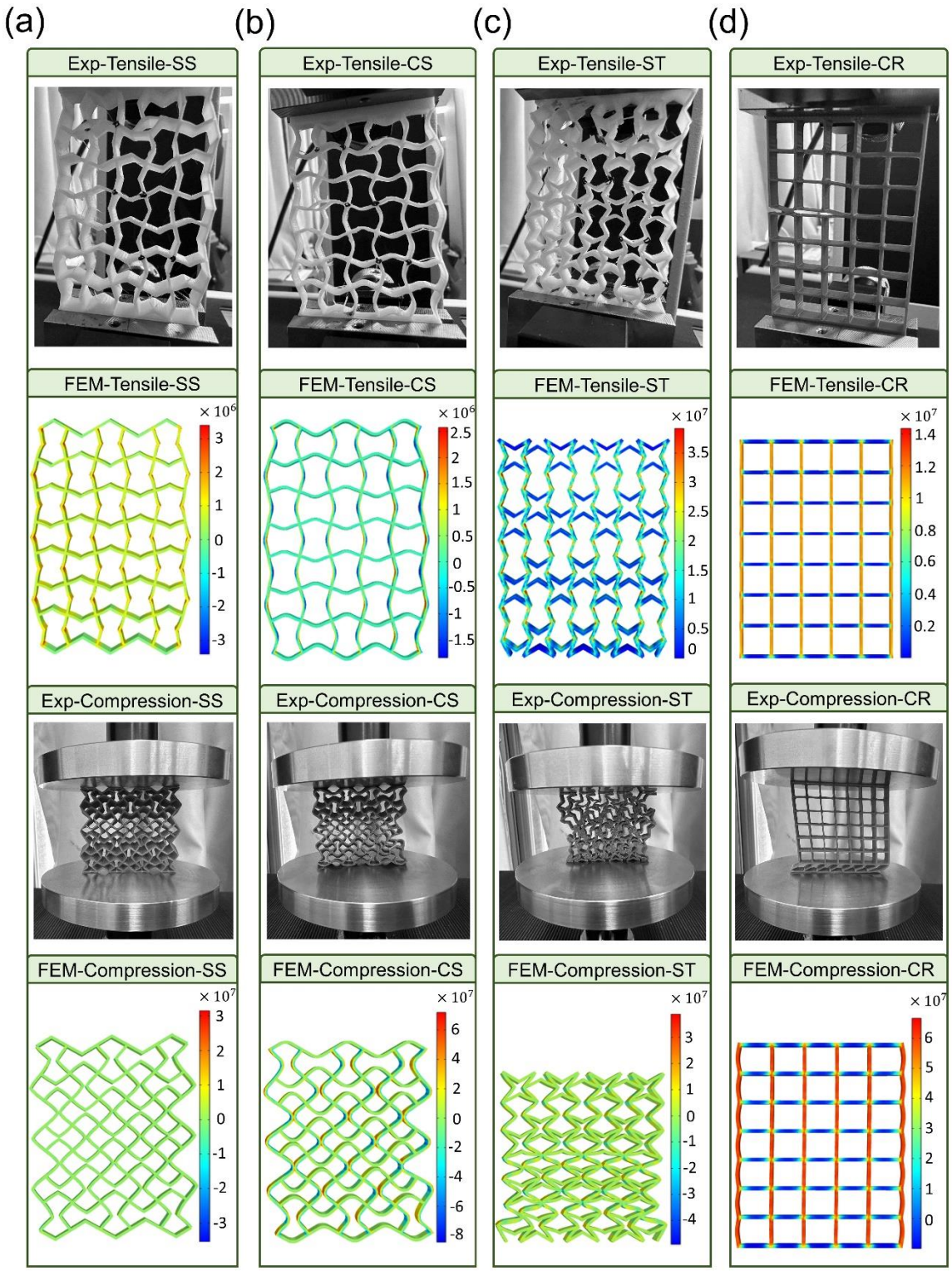

Figure 3. Tensile and compressive investigations of (a) SS, (b) CS, (c) ST, and (d) CR scaffolds with FEM (compressive and tensile stress in Pa). Abbreviations: Exp, experiment; FEM, finite element method; SS, sharp sinus; CS, curved sinus; ST, star; CR, conventional rectangular.

Furthermore, FEM was implemented in this study to analyze the mechanical properties of auxetic and conventional structures comprehensively. As presented in Figure 2(b-i), the FEM accurately predicted the mechanical properties of the scaffolds and closely mirrored the experimental results. In addition, a mesh sensitivity analysis was conducted to determine the optimal mesh size, ensuring that the results were robust and independent of the mesh size chosen. Moreover, leveraging FEM allowed for the assessment of stress distribution within the porous structures, which was critical for identifying vulnerable regions. It also precisely indicated the contraction and expansion mechanisms inherent to auxetic structures, offering insights into their ability to withstand significant deformations and demonstrate exceptional energy absorption. Notably, all three auxetic structures with inclined struts effectively managed external loads under both tensile and compressive conditions. However, the CR structure solely relied on its vertical struts to withstand external forces, raising the risk of sudden cracks under low strain (Figure 3).

2.2. Dynamic (Fatigue) Tensile and Compressive Properties of Scaffolds

To assess the long-term effectiveness and durability of the scaffolds, fatigue properties were investigated under cyclic loads [9b, 11a]. Real tendons exhibit varying numbers of cycles to failure depending on the proximity of the load to the ultimate tensile strength [18], and they should also tolerate compressive loads in the human body [19]. In this study, both compressive and tensile cyclic loads were considered to evaluate the dynamic mechanical properties of the auxetic (SS, CS, CT) and conventional (CR) structures. As presented in Figure 4 and 5, fatigue properties were calculated under high, moderate, and low stress for each scaffold, and the strain accumulation behavior was analyzed for different stress levels. In tensile loading, the auxetic structures extended parallel to the external force, forming semi-vertical struts and increasing stress within the scaffolds. As the tensile load increased, the second and third layers encountered similar conditions, and the strain gradually shifted from inclined struts to vertical struts, enabling effective damping of tension-tension loads within auxetic structures (Figure 4a, b, and c).

Among all the designs, the ST scaffold, characterized by a lower level of auxeticity, exhibited higher resistance to failure, demonstrating its ability to withstand tension-tension loads in low, moderate, and high-force levels. This observation indicates that the effect of auxeticity should be considered in the investigation of fatigue properties of porous structures [20]. In the case of SS and

CS structures, the weakest regions were identified at the end of the inclined struts, primarily due to the considerable bending moments in those regions [21]. Including supporting struts in the ST structure mitigated extensive bending, consequently augmenting its resistance to failure. Moreover, according to the beam theory, external force can cause deformations in scaffolds. In SS and CS structures, the deformation in inclined struts is controlled by two beams; however, it is mitigated by three struts, which can decrease the deformation and control the stress better [22].

In parallel with experimental assessments, FEM was harnessed to predict cycles to failure in auxetic and conventional structures, as shown in Figure 4e. The history of static loads was used in the simulations, primarily focused on tension-tension loading [23]. The red regions in Figure 4e highlight the most critical zones vulnerable to failure under tension-tension loads. The experimental and numerical results in Figure 4e demonstrate the accuracy of the FEM predictions under the highest tension loads. For instance, while the conventional structure was predicted to endure only 10 cycles to failure under the highest tensile loads, approximately 50, 100, and 50 cycles to failure were estimated by FEM for SS, CS, and ST, respectively. Interestingly, the ST structure exhibited a notable pattern, with the red regions deviating from straight lines and intersecting with the green regions, implying its potential to withstand more cycles than 50, which corresponds to the lowest number of cycles to failure predicted by FEM for the ST structure. Furthermore, the cracked regions in actual tension-tension tests, highlighted by the dot lines in Figure 4e, closely corresponded to the locations of the weakest red zones identified by FEM. The congruence between the observed number of cycles to failure under the highest loads and the prediction from FEM for the weakest regions validated the accuracy of the results.

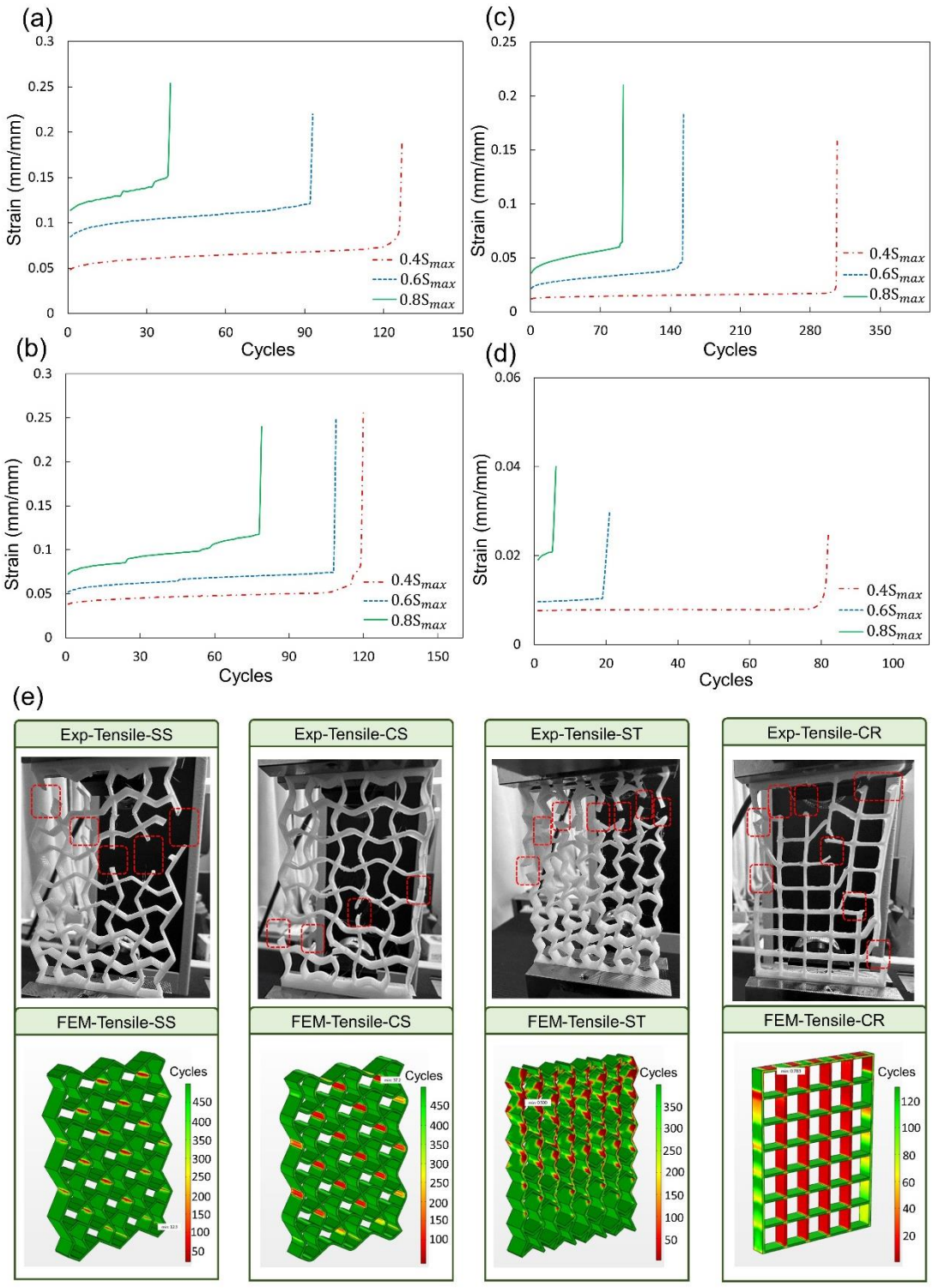

Figure 4. Strain accumulation curves of (a) SS, (b) CS, (c) ST, and (d) CR under dynamic tension-tension loads. (e) Cracked regions (dotted red line) under tension-tension dynamic tests and FEM prediction. Abbreviations: S_{max}, maximum stress; Exp, experiment; FEM, finite element method; SS, sharp sinus; CS, curved sinus; ST, star; CR, conventional rectangular.

Compression-compression strain-cycles graphs typically have three main stages: increasing strain, constant strain, and rapid accumulation of strain leading to cracks [11a, 24]. As presented in Figure 5a-d, while several unusual jumps were observed in strain-cycles graphs of auxetic structures, the CR structure exhibited a constant accumulation in the first and second stages, followed by a sudden elevation. This phenomenon stems from the buckling pattern observed in the conventional structure. Under the increased load via the universal testing machine (UTM), the vertical struts in the CR structure were primarily deformed, eventually leading to a critical point and sudden failure [25]. In contrast, the auxetic structures displayed unique behavior, where inclined struts moved closer to each other under compression, resulting in densification regions (Figure 3a-c). This layer-by-layer densification caused jumping and damping regions in the strain-cycles graph, with such occurrences originating from the deformation of inclined struts [24].

Notably, there were considerable differences in the number of cycles between auxetic and conventional structures in compression-compression fatigue tests due to the buckling pattern of the compressive load. The inclined struts effectively controlled the buckling pattern in auxetic structures, which is characterized by the increasing and damping strain level in strain-cycles graphs in Figure 5a, b, and c. Furthermore, the level of auxeticity was found to relate to the scaffold's compression-compression behavior [26]. The SS and CS structures with a lower negative Poisson's ratio showed a higher number of cycles to failure than the ST design under high and moderate loads. This suggests that higher auxeticity could enhance the number of cycles to failure under compression-compression fatigue loads. However, in the tensile-tensile test, auxeticity should be controlled carefully to extensively enhance the fatigue properties. These results underscore that Poisson's ratio can play a crucial role in improving the fatigue properties of porous architectures under compression-compression loads.

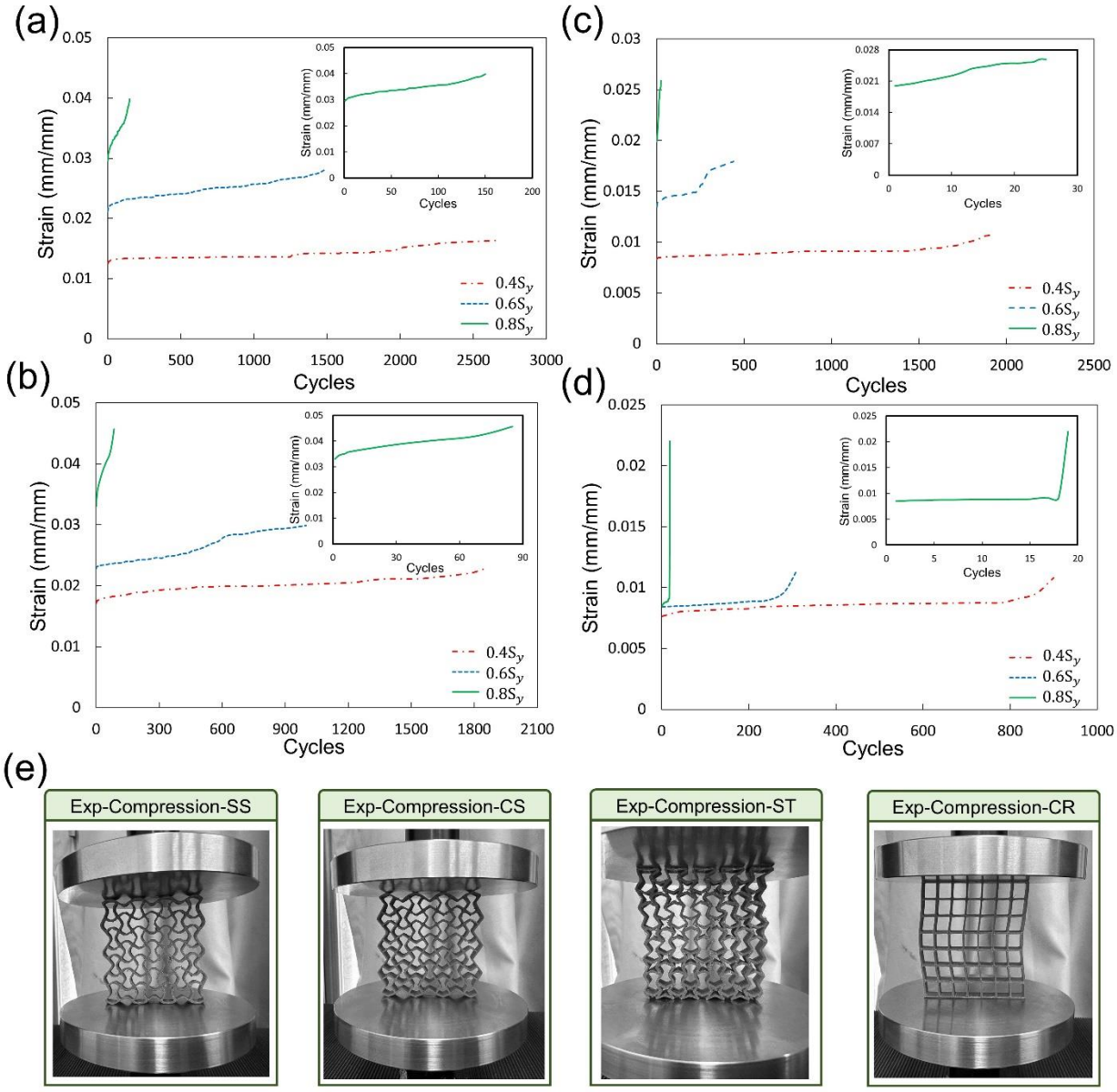

Figure 5. Strain accumulation curves of (a) SS, (b) CS, (c) ST, and (d) CR under dynamic compression-compression loads. (e) Deformation under compression-compression loads. Abbreviations: S_y: yield strength; Exp, experiment; SS, sharp sinus; CS, curved sinus; ST, star; CR, conventional rectangular.

To comprehensively compare the fatigue properties of the scaffolds, graphs of maximum force versus cycles were provided in Figure 6 for both tension-tension and compression-compression loads. The ST structure could tolerate the highest tension-tension loads despite the influence of lower porosity on its fatigue properties. The SS and CS structures further supported the assertion

that the auxetic designs exhibited superior fatigue properties compared to the CR architecture. For instance, the CR structure could tolerate 82 cycles under the lowest tensile force of 285 N, while the SS and CS structures endured 93 and 109 cycles under forces of 354 N and 289 N, respectively. The ST scaffolds withstood even higher forces of 380 N and 153 cycles. These results confirmed the superior energy absorption and higher capacity of the auxetic structures to bear tension-tension cyclic loads.

In contrast, comparing the results of compression-compression tests is more challenging due to the sudden failure in the CR structures. As previously mentioned, the compression-compression experimental tests were stopped upon a 30% increase in strain. In the CR structure, as shown in Figure 5d, the strain remained constant and suddenly elevated, making it difficult to achieve the 30% increase in strain. However, as shown in Figure 6b, the slope of the force versus cycles in CR illustrated how the increasing force could weaken its fatigue properties. Conversely, the slope in SS, CS, and ST structures demonstrated a lower dependency of cycles to force in compression-compression tests, suggesting that increasing force had a lesser impact on the fatigue properties of auxetic samples. These structures demonstrated an ability to tolerate high cycles under substantial compression loads compared to conventional scaffolds.

Although this study effectively focused on biomimicking the physical and mechanical properties of natural tendons using auxetic structures, future studies should investigate the impact of different materials on the fatigue properties of auxetic structures. This avenue of exploration could lead to further enhancements in the static and dynamic mechanical characteristics of bioinspired auxetic architectures, contributing to their continuous improvement and broader applicability. Furthermore, the present study can be utilized in different topics that are susceptible to cyclic loads requiring high energy absorption, such as soft robotics. One of the important problems in soft robotics is their weakness in tolerating cyclic loads, which can be compensated by the present design and improve their number of cycles versus life. Besides this positive impact, the high energy absorption of auxetic structures can guarantee the sustainability of soft robotics [27].

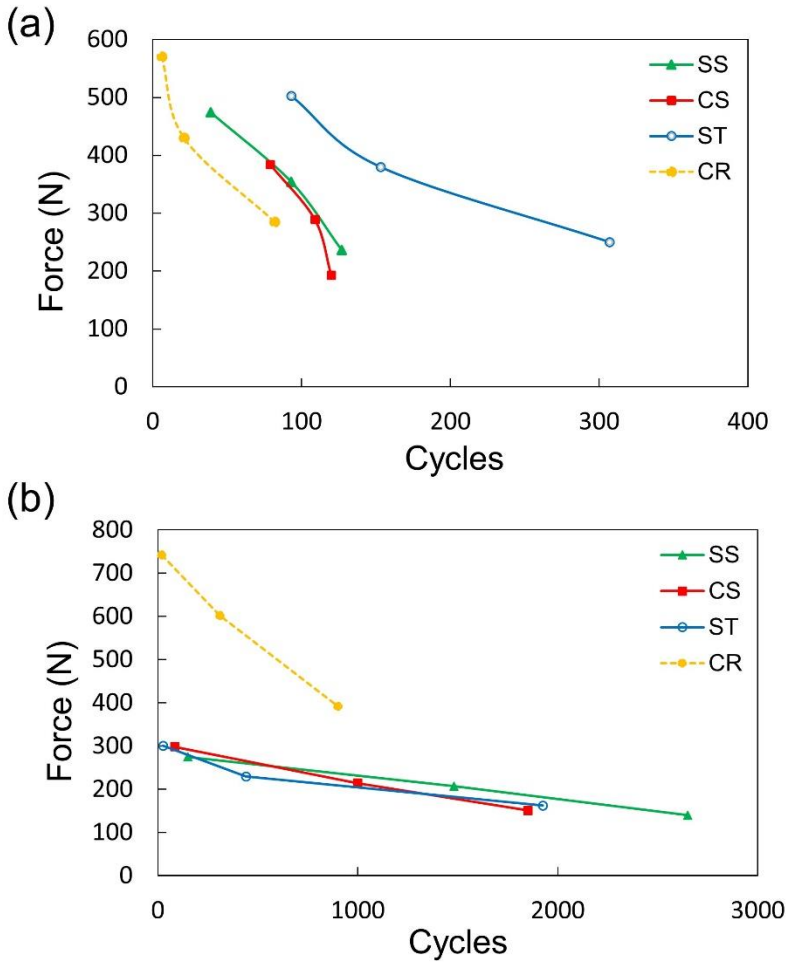

Figure 6. Graphs of maximum force versus cycles in (a) tension-tension and (b) compression-compression dynamic tests. Abbreviations: SS, sharp sinus; CS, curved sinus; ST, star; CR, conventional rectangular.

3. Conclusion

In conclusion, this study fabricated and compared three bioinspired auxetic structures and one conventional architecture using 3D printing with PLA material. The results demonstrated that the bioinspired auxetic structures effectively mimic the tensile behavior of human tendons and outperform the conventional structure in terms of tolerating cyclic tests under tension-tension and compression-compression loads. The auxetic structures showed a significant increase in the number of cycles to failure, almost three times higher than the conventional design. Additionally, the auxetic structures' energy absorption was two to three times greater than that of the conventional architecture. Notably, the mechanical properties of the bioinspired auxetic structures exhibited considerable variations when subjected to different static and dynamic loads, indicating

that the tensile and compression behaviors of materials do not follow similar patterns. Also, slight modifications in the design of unit cells had a considerable impact on the overall mechanical properties of the structures, as demonstrated in the comparison between the SS and CS structures. Furthermore, the FEM analysis revealed that the conventional structure had a lower stress distribution capacity, with only the vertical struts enduring loads. In contrast, the auxetic structures utilized all struts to withstand external loads, thereby improving their overall performance.

4. Experimental Methods

As depicted in Figure 1, the study involved the investigation of 3D bioinspired scaffolds using a combination of experimental and numerical approaches, considering tensile and compressive loads in both static and dynamic conditions. The design and evaluation of these structures were inspired by the real tissue properties and normal life conditions. Natural tendons have a crimp structure with a negative Poisson's ratio. However, the level of auxeticity and mechanical properties in natural tendons can be varied in different cases. For instance, the Poisson's ratio of the Achilles tendon falls within -0.39 to -1.44, and their elastic modulus can be 2 GPa to 140 MPa. Other tendons follow the same situation with various auxeticity and mechanical properties. Based on the morphological and mechanical properties of natural tendons, three different structures were designed and fabricated to be implemented for various cases [6a, 28].

Design and 3D Printing of Scaffolds: In this study, filaments made of polylactic acid (PLA; Sindoh Co.), a biocompatible polymer with suitable mechanical properties for biomedical applications, were used with an FDM 3D printer (Sindoh Co.) to fabricate different auxetic and conventional structures. Specifically, three auxetic structures and one conventional rectangular architecture were designed and fabricated. All scaffolds were printed with a 0.4 mm nozzle diameter at 200 °C. In this machine, the bed temperature was set to 60 °C. The conventional rectangular structure served as a control for comparison with the auxetic designs. It was carefully designed to share the same step size as the auxetic structures and maintain nearly equivalent porosity to mitigate the influence of porosity on the mechanical properties of scaffolds. Comprehensive details regarding the unit cell designs and dimensions are illustrated in Table 3 and Figure 7. The height of all printed structures was set to 5 mm, and they were denoted as SS, CS, ST, and CR.

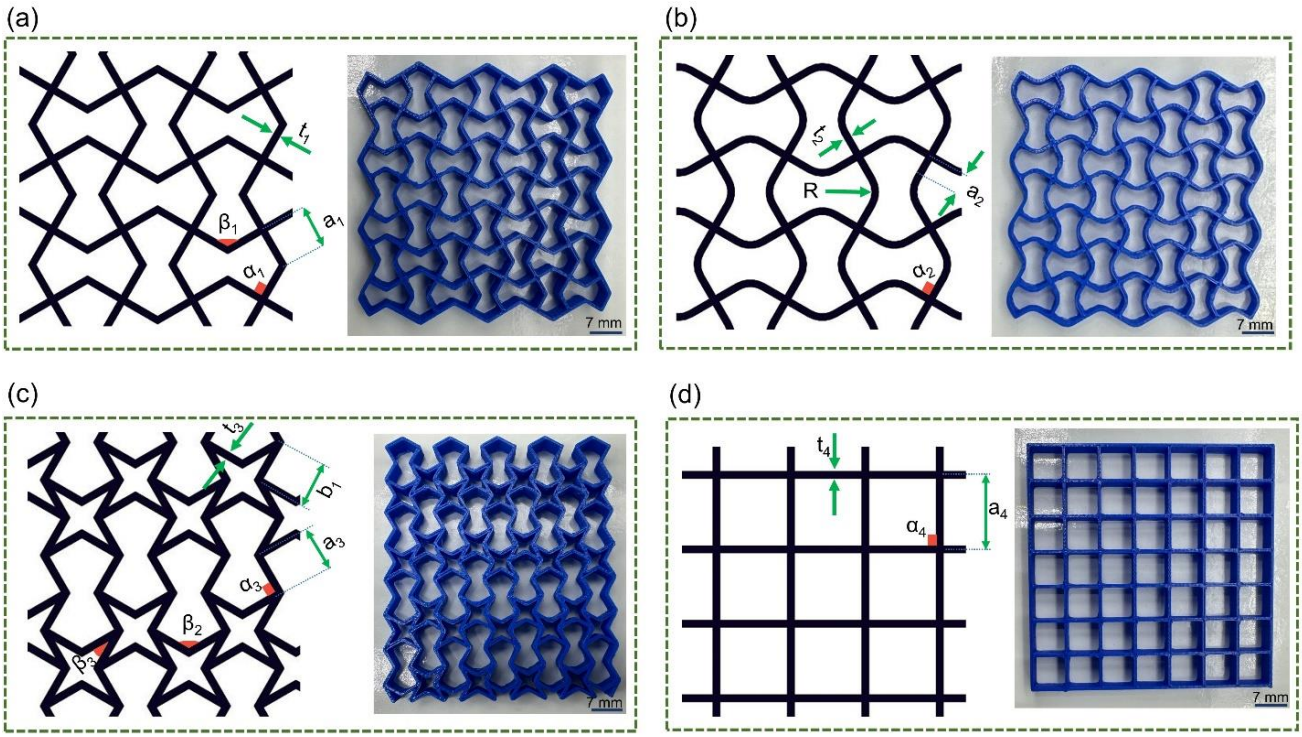

Figure 7. Different designs of unit cells. (a) SS, (b) CS, (c) ST, and (d) CR. Abbreviations: SS, sharp sinus; CS, curved sinus; ST, star; CR, conventional rectangular.

Table 3. Dimensions of structures.

Structure	SS	CS	ST	CR
a_1 (mm)	5	-	-	-
a_2 (mm)	-	3.27	-	-
a_3 (mm)	-	-	5	-
a_4 (mm)	-	-	-	7.86
b_1 (mm)	-	-	5	-
t_1 (mm)	0.8	-	-	-
t_2 (mm)	-	0.8	-	-
t_3 (mm)	-	-	0.8	-
t_4 (mm)	-	-	-	0.8
R (mm)	-	3	-	-
α_1 (°)	90	-	-	-
α_2 (°)	-	90	-	-
α_3 (°)	-	-	90	-
α_4 (°)	-	-	-	90
β_1 (°)	120	-	-	-
β_2 (°)	-	-	120	-
β_3 (°)	-	-	30	-

Abbreviations: SS, sharp sinus; CS, curved sinus; ST, star; CR, conventional rectangular.

Assessment of Static Mechanical Properties: Compressive and tensile tests were conducted on bulk samples using a universal testing machine (LR5K plus, LLOYD Instruments) equipped with a 5 kN load cell to comprehensively evaluate the mechanical properties of the scaffolds. The bulk samples were designed using the ASTM D695 standard for compression and ASTM D638 for the tensile tests. This strategy was also employed to calculate the static mechanical properties of porous scaffolds. Additionally, the speed of the head of the UTM was set to 1 mm/min, ensuring at least a 20% increase or decrease in the specimens' height during testing. To validate the experimental outcomes, each test was repeated three times. The stress-strain curves of the compression and tensile tests were plotted based on the apparent stress and non-dimensional strain. The yield stress was computed using the 0.2% offset method. A mounted camera was deployed to capture images and assess the Poisson's ratio of the auxetic and rectangular scaffolds. Also, the following equations were utilized to calculate the Poisson's ratio (υ_{xy}), where ε_x and ε_y are the strain in the x-axis and y-axis directions, Δ_x and Δ_y denote deformation in the x-axis and y-axis directions, and l_{x0} and l_{y0} represent the initial distances between reference points before elongation.

$$\varepsilon_x = \frac{\Delta_x}{l_{x0}} \tag{1}$$

$$\varepsilon_y = \frac{\Delta_y}{l_{y0}} \tag{2}$$

$$\upsilon_{xy} = -\frac{\varepsilon_x}{\varepsilon_y} \tag{3}$$

Fatigue Test: Tension-tension and compression-compression fatigue tests were conducted using the same machine as the static tests, with a 5 kN load cell. The strain rate of the loading was fixed at 1 mm/min for both tests, and the load ratio was set to R = 0.1 to establish a relation between maximum and minimum loads. It should be noted that vibration has a great impact on mechanical response in metamaterials; however, the present study utilizes low-frequency tests to follow low frequency tolerated by human during a normal life [29]. For each porous structure, three different values of the maximum force were selected based on high stress (0.8 σ_{max}), low stress (0.4 σ_{max}), and moderate stress (0.6 σ_{max}), with σ_{max} replaced by the yield stress in compression-compression tests (Table 1). The tension-tension fatigue test continued until failure, while the compression-compression fatigue test stopped at a 30% increase in the first strain to account for

the densification effect, thereby increasing the number of cycles to failure and the test time. To ensure accuracy, each fatigue test was repeated at least twice. If the number of cycles to failure varied extensively (more than 40%), a third repetition was performed. The strain-cycle curve was used to analyze the effect of cyclic forces on the porous structure scaffolds. All the graphs were prepared for both the tension-tension and compression-compression loading conditions.

*FEM Simulations***:** The static and fatigue properties of the scaffolds were investigated using the FEM software (COMSOL Multiphysics, COMSOL Inc.). CAD models were imported into the FEM software, and similar boundary conditions as in the experimental part were applied to the model. A 3D structural element (tetrahedral) was utilized to mesh the 3D structures based on the shape of the scaffolds. This procedure was repeated for all the designs, and a sensitivity analysis was performed for each scaffold to determine the optimum element numbers.

The fatigue module of FEM software with the strain-based option was employed to predict the cycle to failure of the SS, CS, ST, and CR structures. The strain-based analysis required specific coefficients and the loading history in a static situation. To achieve this, previously published data was imported to set fatigue coefficients of the simulation, and the history of the static loads was utilized by defining three loading stages, as outlined in the reference [30]. In the initial stage, the load was incrementally raised from zero to F_{max}, subsequently decreasing to F_{min} to simulate a cyclic procedure. After running the load history step, the results were utilized in the fatigue module, enabling COMSOL to predict the number of cycles to failure and identify the weakest regions under dynamic loads.

Acknowledgment

This research was supported by a National Research Foundation of Korea (NRF) grant (NRF-2021R1I1A3040459) funded by the Korean government (MOE). This research was supported by a grant of the Korea Health Technology R&D Project through the Korea Health Industry Development Institute (KHIDI), funded by the Ministry of Health & Welfare, Republic of Korea (grant number: HI22C1323). This work was also supported by the UK Engineering and Physical Sciences Research Council (EPSRC) [grant number EP/Y011457/1].

References

[1] a) V. A. Lvov, F. S. Senatov, A. A. Veveris, V. A. Skrybykina, A. Díaz Lantada, *Materials* **2022**, 15, 1439; b) C. Wang, Z. Vangelatos, C. P. Grigoropoulos, Z. Ma, *Materials Today Advances* **2022**, 13, 100206.

[2] R. P. Bohara, S. Linforth, T. Nguyen, A. Ghazlan, T. Ngo, *International Journal of Mechanical Sciences* **2021**, 211, 106793.

[3] a) D. Tahir, M. Zhang, H. Hu, *physica status solidi (b)* **2022**, 2200324; b) A. A. Morin-Martinez, J. Arcudia, X. Zarate, M. E. Cifuentes-Quintal, G. Merino, *Journal of Computational Chemistry* **2023**, 44, 248.

[4] a) M. Shirzad, A. Zolfagharian, M. Bodaghi, S. Y. Nam, *European Journal of Mechanics-A/Solids* **2022**, 104905; b) O. Duncan, T. Shepherd, C. Moroney, L. Foster, P. D. Venkatraman, K. Winwood, T. Allen, A. Alderson, *Applied Sciences* **2018**, 8, 941; c) M. Shirzad, M. Bodaghi, D. Oh, M. Yi, S. Y. Nam, *European Journal of Mechanics-A/Solids* **2024**, 103, 105139.

[5] a) H. M. Kolken, S. Janbaz, S. M. Leeflang, K. Lietaert, H. H. Weinans, A. A. Zadpoor, *Materials Horizons* **2018**, 5, 28; b) P. Chansoria, J. Blackwell, E. L. Etter, E. E. Bonacquisti, N. Jasiewicz, T. Neal, S. A. Kamal, J. Hoque, S. Varghese, T. Egan, *Advanced Functional Materials* **2022**, 32, 2207590.

[6] a) R. Gatt, M. V. Wood, A. Gatt, F. Zarb, C. Formosa, K. M. Azzopardi, A. Casha, T. P. Agius, P. Schembri-Wismayer, L. Attard, *Acta biomaterialia* **2015**, 24, 201; b) M. Shirzad, A. Matbouei, A. Fathi, S. M. Rabiee, *Proceedings of the Institution of Mechanical Engineers, Part L: Journal of Materials: Design and Applications* **2020**, 234, 586.

[7] N. Chikkanna, K. P. Logakannan, S. Krishnapillai, V. Ramachandran, *Thin-Walled Structures* **2022**, 179, 109550.

[8] a) R. Hedayati, A. Yousefi, M. L. Dezaki, M. Bodaghi, *Journal of the Mechanical Behavior of Biomedical Materials* **2023**, 143, 105938; b) Y. Wu, B. Wu, S. Vijayavenkataraman, Y. San Wong, J. Y. H. Fuh, *Materials & Design* **2017**, 131, 384; c) J. J. Warner, A. R. Gillies, H. H. Hwang, H. Zhang, R. L. Lieber, S. Chen, *Journal of the mechanical behavior of biomedical materials* **2017**, 76, 145; d) V. Russo, M. El Khatib, L. di Marcantonio, M. Ancora, R. Wyrwa, A. Mauro, T. Walter, J. Weisser, M. R. Citeroni, F. Lazzaro, *Cells* **2020**, 9, 303.

[9] a) D. Zhao, Y. Huang, Y. Ao, C. Han, Q. Wang, Y. Li, J. Liu, Q. Wei, Z. Zhang, *Journal of the mechanical behavior of biomedical materials* **2018**, 88, 478; b) L. Zhu, H. Liang, F. Lv, D. Xie, C. Wang, Y. Mao, Y. Yang, Z. Tian, L. Shen, *ACS Biomaterials Science & Engineering* **2021**, 7, 1663.

[10] a) S. A. Yavari, S. Ahmadi, R. Wauthle, B. Pouran, J. Schrooten, H. Weinans, A. Zadpoor, *Journal of the mechanical behavior of biomedical materials* **2015**, 43, 91; b) S. Ahmadi, R. Hedayati, Y. Li, K. Lietaert, N. Tümer, A. Fatemi, C. Rans, B. Pouran, H. Weinans, A. Zadpoor, *Acta biomaterialia* **2018**, 65, 292.

[11] a) Z. Liu, H. Gong, J. Gao, *International Journal of Mechanical Sciences* **2023**, 108119; b) M. Zhao, X. Li, D. Z. Zhang, W. Zhai, *International Journal of Mechanical Sciences* **2023**, 238, 107842.

[12] a) A. A. Soufivand, N. Abolfathi, S. A. Hashemi, S. J. Lee, *Additive Manufacturing* **2020**, 33, 101181; b) M. Shirzad, A. Fathi, S. M. Rabiee, S. Ghaffari, E. Zabihi-Neishabouri, *Proceedings of the Institution of Mechanical Engineers, Part C: Journal of Mechanical Engineering Science* **2020**, 234, 3133; c) Z. Fan, G. Huang, Y. Lu, Y. Chen, F. Zeng, J. Lin, *International Journal of Mechanical Sciences* **2022**, 223, 107294.

[13] a) M. Shirzad, A. Zolfagharian, A. Matbouei, M. Bodaghi, *Journal of the mechanical behavior of biomedical materials* **2021**, 120, 104594; b) H. K. Chang, D. H. Yang, M. Y. Ha, H. J. Kim, C. H. Kim, S. H. Kim, J. W. Choi, H. J. Chun, *Carbohydrate Polymers* **2022**, 287, 119328; c) K. Choi, C. Y. Park, J. S. Choi, Y.-J. Kim, S. Chung, S. Lee, C.-H. Kim, S. J. Park, *Tissue Engineering and Regenerative*

Medicine **2023**, 1; d) H. Lee, J. M. Yoo, N. K. Ponnusamy, S. Y. Nam, *Ceramics International* **2022**, 48, 10155.
[14] a) A. Grémare, V. Guduric, R. Bareille, V. Heroguez, S. Latour, N. L'heureux, J. C. Fricain, S. Catros, D. Le Nihouannen, *Journal of Biomedical Materials Research Part A* **2018**, 106, 887; b) M. Mohammadi-Zerankeshi, R. Alizadeh, *Journal of Materials Research and Technology* **2023**, 22, 2440.
[15] J. H.-C. Wang, *Journal of biomechanics* **2006**, 39, 1563.
[16] a) T. Almela, I. M. Brook, K. Khoshroo, M. Rasoulianboroujeni, F. Fahimipour, M. Tahriri, E. Dashtimoghadam, A. El-Awa, L. Tayebi, K. Moharamzadeh, *Bioprinting* **2017**, 6, 1; b) J. Williams, J. Lewis, **1982**.
[17] S. Li, Y.-w. Kim, M.-s. Choi, T.-h. Nam, *Intermetallics* **2020**, 116, 106657.
[18] H. Schechtman, D. Bader, *Journal of biomechanics* **1997**, 30, 829.
[19] I. Bah, S. T. Kwak, R. L. Chimenti, M. S. Richards, J. P. Ketz, A. S. Flemister, M. R. Buckley, *Journal of the mechanical behavior of biomedical materials* **2016**, 53, 320.
[20] a) L. Francesconi, A. Baldi, G. Dominguez, M. Taylor, *Experimental Mechanics* **2020**, 60, 93; b) A. Bezazi, F. Scarpa, *International Journal of Fatigue* **2009**, 31, 488.
[21] B. Nečemer, T. Vuherer, S. Glodež, J. Kramberger, *Thin-Walled Structures* **2022**, 180, 109917.
[22] R. Hedayati, M. Sadighi, M. Mohammadi-Aghdam, A. Zadpoor, *Materials Science and Engineering: C* **2016**, 60, 163.
[23] V. Lvov, F. Senatov, A. Stepashkin, A. Veveris, M. Pavlov, A. Komissarov, *Materials Today: Proceedings* **2020**, 33, 1979.
[24] H. Kolken, A. F. Garcia, A. Du Plessis, C. Rans, M. Mirzaali, A. Zadpoor, *Acta Biomaterialia* **2021**, 126, 511.
[25] S. Zhao, S. Li, W. Hou, Y. Hao, R. Yang, R. Misra, *Journal of the mechanical behavior of biomedical materials* **2016**, 59, 251.
[26] J. Michalski, T. Strek, presented at Advances in Manufacturing II: Volume 4-Mechanical Engineering **2019**.
[27] a) H. Soleimanzadeh, B. Rolfe, M. Bodaghi, M. Jamalabadi, X. Zhang, A. Zolfagharian, *Advanced Sustainable Systems* **2023**, 7, 2300289; b) M. Bodaghi, N. Namvar, A. Yousefi, H. Teymouri, F. Demoly, A. Zolfagharian, *Smart Materials and Structures* **2023**, 32, 095028.
[28] M. Franchi, M. Fini, M. Quaranta, V. De Pasquale, M. Raspanti, G. Giavaresi, V. Ottani, A. Ruggeri, *Journal of anatomy* **2007**, 210, 1.
[29] a) A. Zolfagharian, P. Picken, M. Bodaghi, M. Fard, B. Rolfe, *Advanced Engineering Materials* **2023**, 25, 2300356; b) J. Kala, V. Salajka, P. Hradil, *International Journal of Civil and Environmental Engineering* **2009**, 3, 93; c) E. Shahabpoor, A. Pavic, V. Racic, S. Zivanovic, *Journal of Sound and Vibration* **2017**, 387, 207.
[30] S. Hassanifard, S. M. Hashemi, *Additive Manufacturing* **2020**, 32, 100973.